Supplement of Atmos. Chem. Phys., 26, 12591–12612, 2026
https://doi.org/10.5194/acp-26-12591-2026-supplement

Atmospheric Chemistry and Physics
Open Access

Supplement of

Planetary albedo change exacerbates surface warming: a perspective from cloud-type changes

Ruixue Li et al.

Correspondence to: Jiming Li (lijiming@lzu.edu.cn)

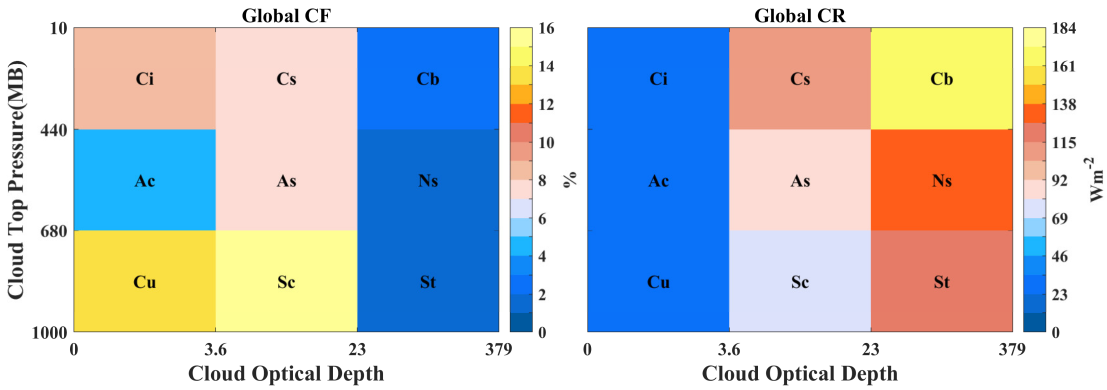

Figure S1. Global mean climatology (January 2003 to December 2022) of the classification of nine cloud types and their properties: (a) cloud fraction (CF), and (b) cloud reflectivity (CR).

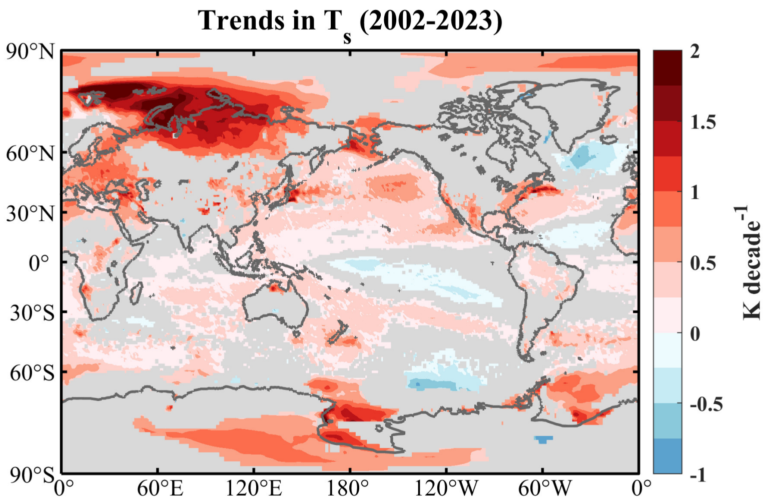

Figure S2. ERA5 decadal surface temperature trends during July 2002 to February 2023 (only grids significant at >95% level shown).

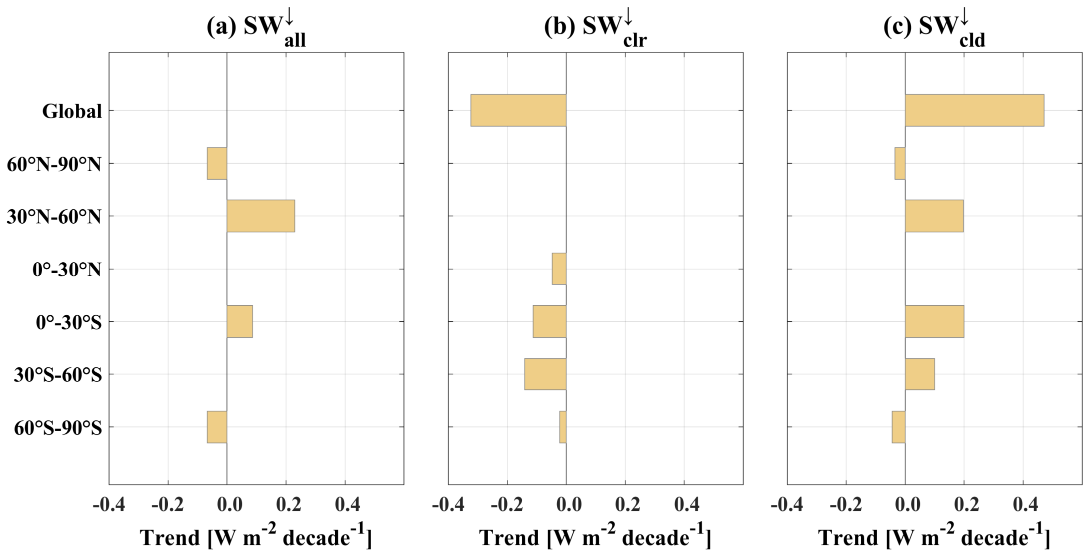

Figure S3. Global and latitude-zone averaged trends in (a) all-sky surface downward shortwave radiation fluxes ($SW_{all}^{\downarrow}$), (b) clear-sky surface downward shortwave radiation fluxes ($SW_{clr}^{\downarrow}$), and (c) the difference between all-sky and clear-sky conditions ($SW_{cld}^{\downarrow} = SW_{all}^{\downarrow} - SW_{clr}^{\downarrow}$). Note that latitudinal-mean trends are area-weighted to account for their contributions to the global mean; the sum of the zonal trends approximately equals the global mean. Only trends significant at the 95% confidence level are shown.

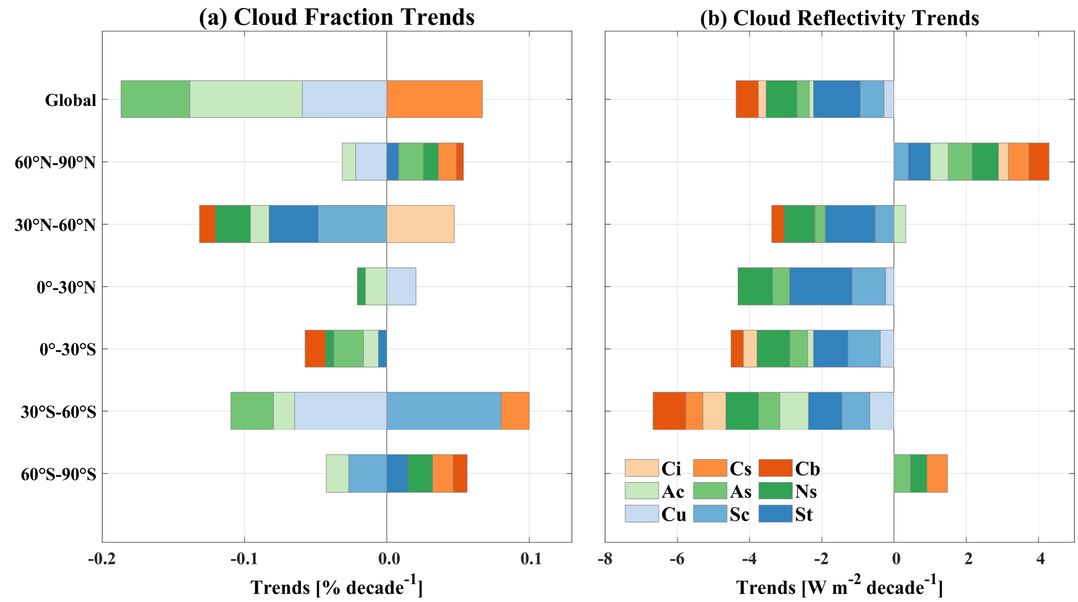

Figure S4. Latitude-zone and global averaged trends (July 2002–February 2023) for (a) CF and (b) CR. The CF trends for each zone are area-weighted to represent global contributions. Only trends significant at the 95% confidence level are shown.

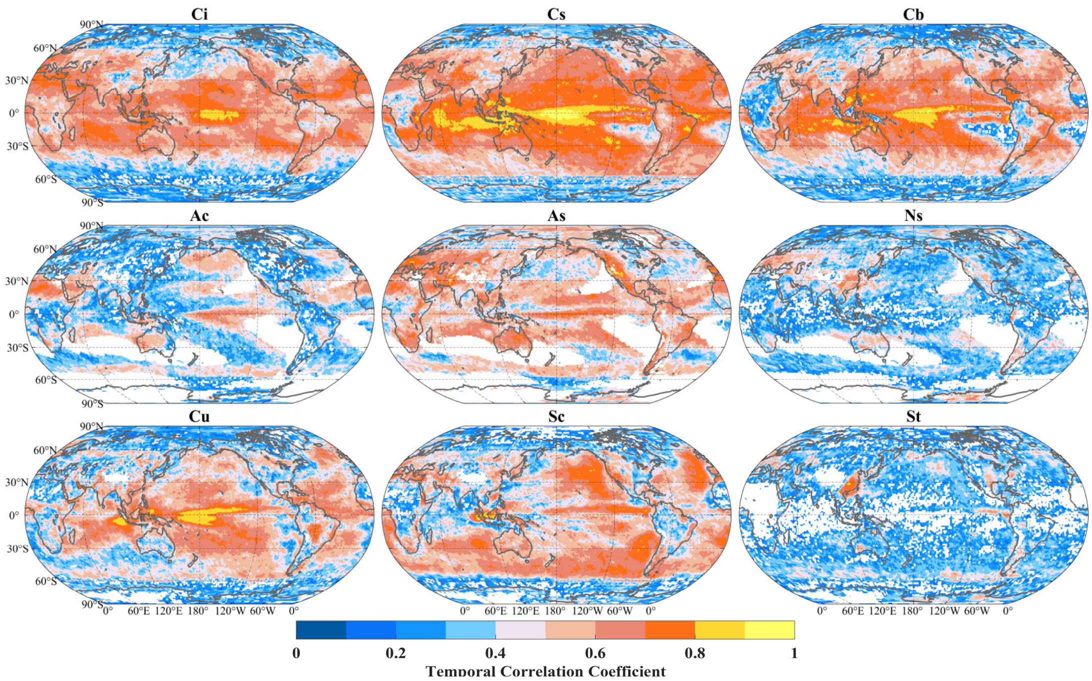

Figure S5. Spatial distribution of the temporal correlation coefficient between the observed and regressed cloud fraction anomalies for nine cloud types.

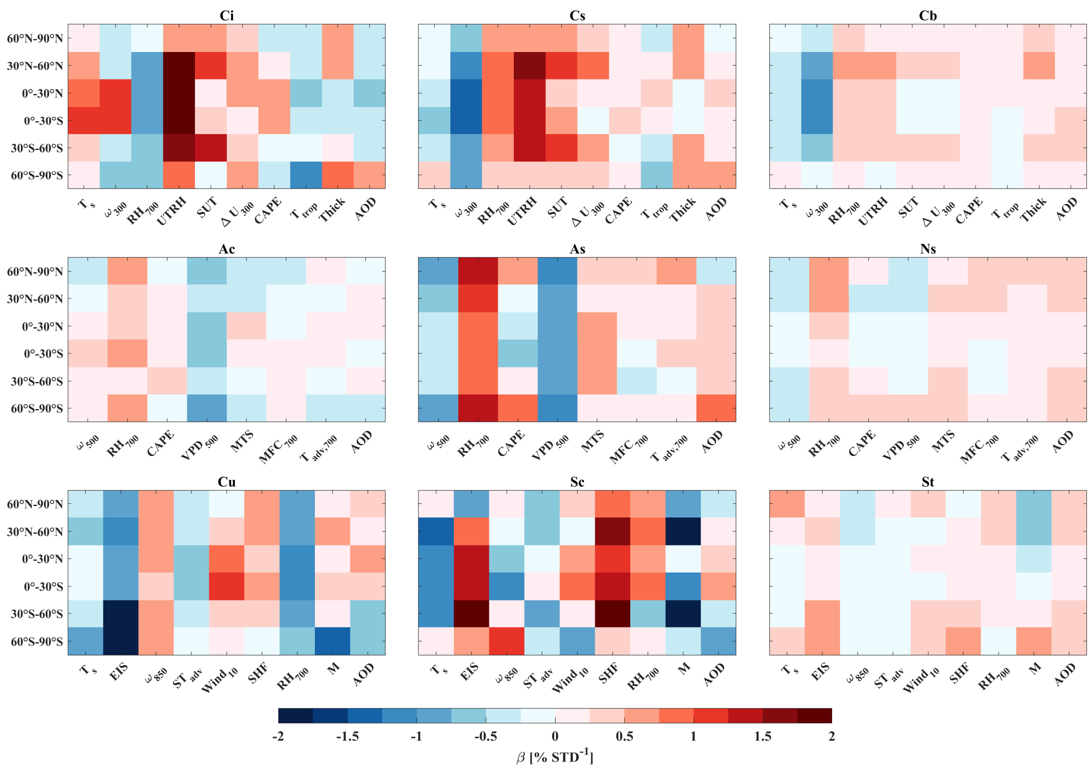

Figure S6. Standardized regression coefficients (β) of cloud controlling factors for nine cloud types across six latitudinal zones.

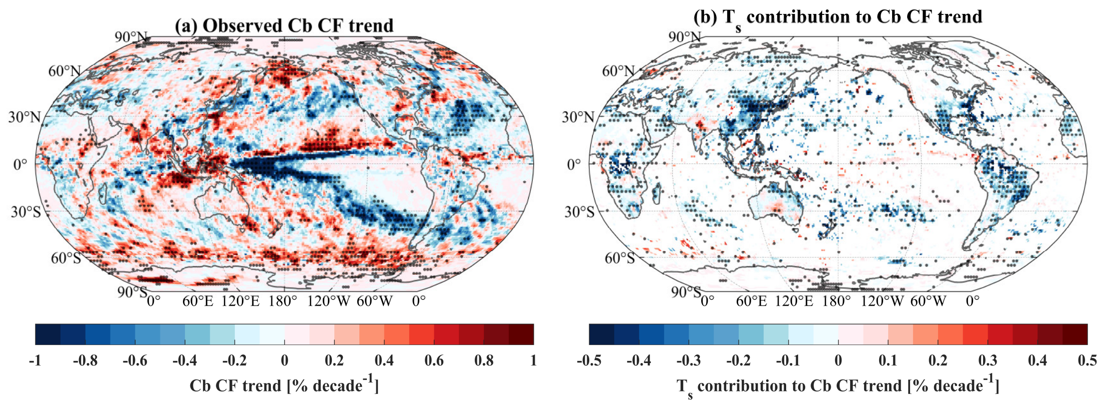

Figure S7. Spatial distributions of (a) the observed trend in cumulonimbus (Cb) cloud fraction and (b) the contribution of surface temperature (T_s) to the Cb cloud-fraction trend over 2002–2023. Black dots indicate trends or contributions significant at the 95% confidence level.

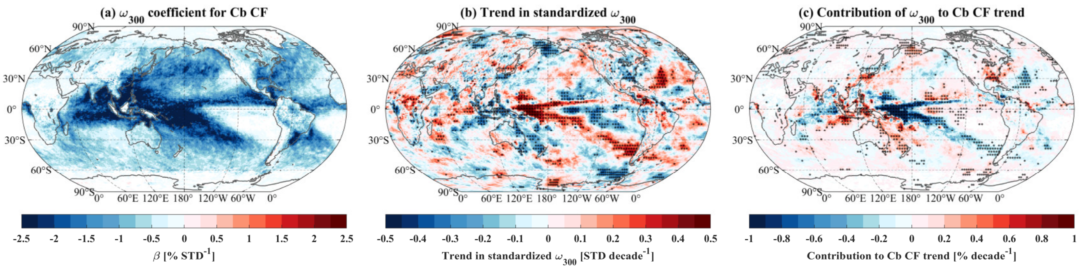

Figure S8. Spatial distributions of (a) the standardized regression coefficient relating 300-hPa pressure vertical velocity (ω_{300}) to Cb cloud fraction, (b) the decadal trend in standardized ω_{300}, and (c) the resulting contribution of ω_{300} to the Cb cloud-fraction trend. Coefficients and contributions are shown where ω_{300} was retained by the stepwise regression. Black dots in (b) and (c) indicate trends significant at the 95% confidence level. Positive ω_{300} trends indicate weakened ascent, whereas negative trends indicate strengthened ascent.

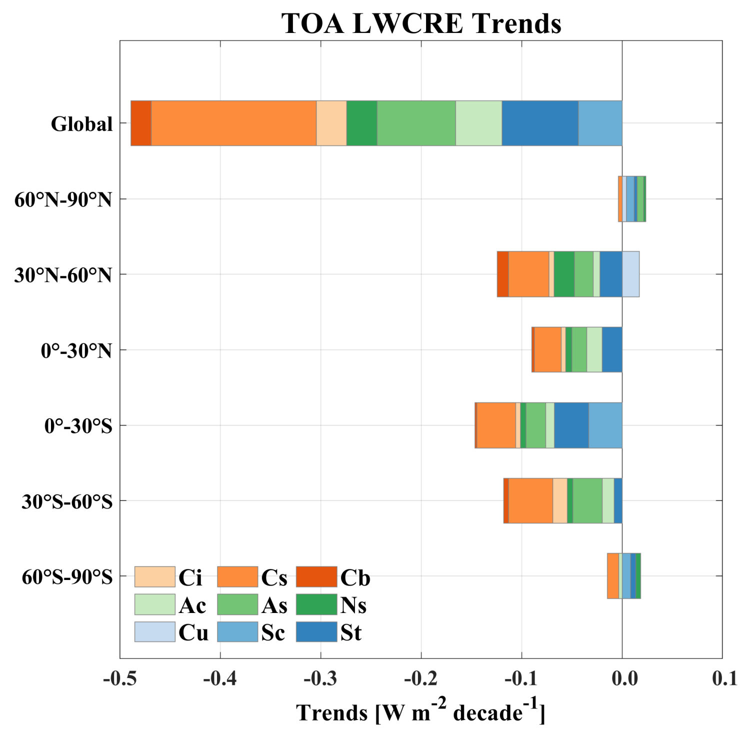

Figure S9. Latitude-zone and global averaged trends (July 2002 to February 2023) for top-of-atmosphere longwave cloud radiative effect (LWCRE). The latitude-zone values are area-weighted to represent their contributions to the global mean. Only trends significant at the 95% confidence level are shown.

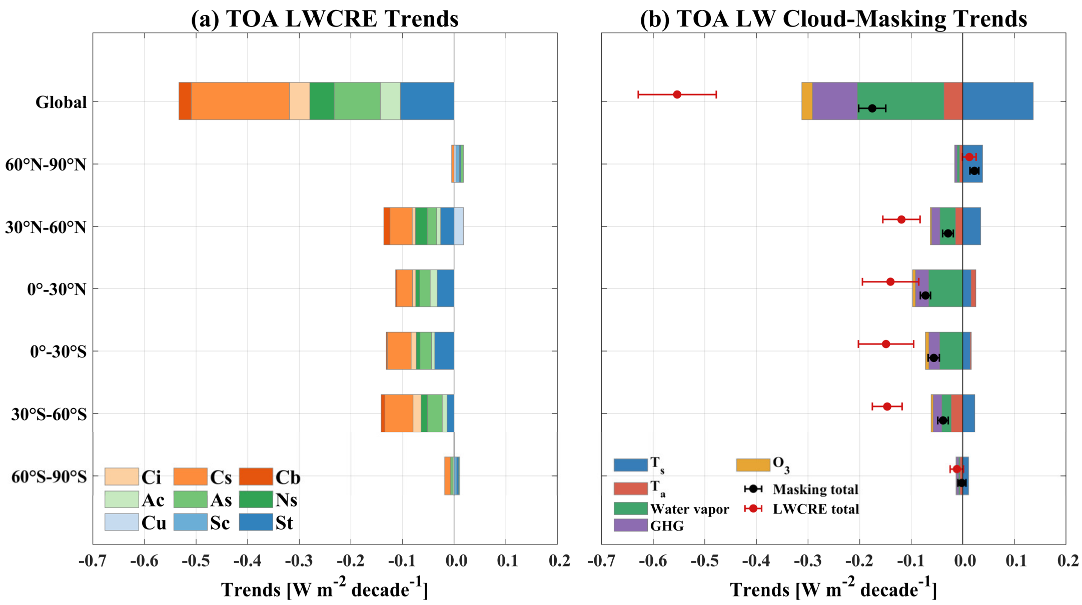

Figure S10. Contributions associated with cloud types and longwave cloud masking to the TOA LWCRE trend from July 2002 to December 2020. (a) Conventional LWCRE trends associated with nine cloud types. Only cloud-type trends significant at the 95% confidence level are shown. (b) Contributions of surface temperature (T_s), atmospheric temperature (T_a), water vapor, well-mixed greenhouse gases (GHGs), and ozone (O_3) to the TOA longwave cloud-masking trend estimated using the ERA5-PRP experiments. Black and red circles denote the total cloud-masking and total LWCRE trends, respectively, with error bars indicating their 95% confidence intervals. Values for the six latitude zones are area-weighted contributions to the global mean, whereas the Global row represents the global-mean trend. Positive values indicate contributions toward increasing LWCRE, and negative values indicate contributions toward decreasing LWCRE.